

# Angular correlation function of the hypersatellite-satellite x-ray cascade following $K$ -shell electron capture of $^{55}\text{Fe}$

Benedikt Bergmann\*

*Institute of Experimental and Applied Physics, Czech Technical University in Prague, Horská 22/3a, 128 00 Praha 2, Czech Republic*

Thilo Michel

*Erlangen Centre for Astroparticle Physics (ECAP), Friedrich-Alexander-Universität Erlangen-Nürnberg, Erwin-Rommel-Straße 1, 91058 Erlangen, Germany*

Andrey Surzhykov and Stephan Fritzsche

*Helmholtz-Institut Jena, Fröbelstieg 3, 07743 Jena, Germany*

(Received 9 March 2016; revised manuscript received 27 May 2016; published 19 July 2016)

The first measurement of the hypersatellite-satellite two-photon angular correlation function following the electron capture decay of  $^{55}\text{Fe}$  was carried out. In particular, two hybrid active pixel detectors were employed to measure the anisotropy parameter  $\beta_2^{\text{eff}}(\text{exp}) = 0.097 \pm 0.053$ , which closely agreed with the theoretical value  $\beta_2^{\text{eff}}(\text{theor}) = 0.09735$ , calculated in the electric-dipole approximation. In addition, we also determined the double  $K$ -shell vacancy creation probability in this specific electron capture decay with improved accuracy. We found  $P_{KK} = (1.388 \pm 0.037) \times 10^{-4}$ , with a systematic error  $\Delta P_{KK, \text{sys}} = 0.042 \times 10^{-4}$ .

DOI: [10.1103/PhysRevC.94.014611](https://doi.org/10.1103/PhysRevC.94.014611)

## I. INTRODUCTION

The capture of an electron by the nucleus usually leaves the atom in an (electronic) hole state with one vacancy in the  $K$  shell. This hole is subsequently filled by electrons from higher shells. Apart from the creation of a single  $K$ -shell hole, there is a small probability  $P_{KK}$  for the second  $K$ -shell electron to be excited to an unoccupied orbital (shake-up) or even to the continuum (shake-off). The probabilities for these shake processes depend on the nuclear charge and are of the order of  $10^{-5}$ – $10^{-4}$ . A “hollow atom,” i.e., an atom with two vacancies in the innermost shell remains. The described electron shake-off is a pure quantum mechanical effect caused by the sudden change in the potential after the electron capture [1]. Theoretically, such shake probabilities are often estimated by means of the overlap of the initial and final wave functions associated with different Hamiltonians.

Such (double)  $K$ -shell vacancies are rapidly filled by electrons from higher shells, which results in an (almost) coincident emission of either two x-ray photons, two Auger electrons, or one x ray together with one Auger electron. Briand *et al.* [2,3] first clearly demonstrated the photons’ shift towards higher energies when compared to the normal  $K$  diagram line photons. If an additional hole occurs in the  $K$  shell, the emitted photon in the transition  $1s^{-2} \rightarrow 1s^{-1}2p^{-1}$  is known as the “hypersatellite” line, while the subsequent photon from  $1s^{-1}2p^{-1} \rightarrow 2p^{-2}$  is called the “satellite.” The energy shifts for these two lines arise from the reduced screening of the Coulomb force of the nuclear charge on the higher-shell electrons caused by the additional vacancy in the innermost shell for the hypersatellite or due to the “spectator” vacancy in the  $L$  shell for the satellite emission.

A first experiment for measuring the probability of creating a double vacancy  $P_{KK}$  in the electron capture of  $^{55}\text{Fe}$  was carried out by Charpak in 1953 by using a pair of gas counters in a coincidence experiment [4]. Since then, several further nuclei have been investigated. An overview of measured values for different nuclei is given in the work of Hindi and Kozub [5]. Most of these measurements were performed with two energy sensitive detectors in coincidence, and they reasonably agree with the theoretical treatment of Primakoff and Porter [6], who predicted a  $Z^{-2}$  behavior of  $P_{KK}$ . However, quite sizable deviations were found for the nuclei  $^{54}\text{Mn}$  and  $^{65}\text{Zn}$  when compared to  $^{55}\text{Fe}$ , as measured by Briand *et al.* [3] and Campbell *et al.* [7]. Michel *et al.* [8] provided a value consistent with the previous measurements, which could resolve the discrepancy for  $^{55}\text{Fe}$  when compared to  $^{54}\text{Mn}$  but not when compared to  $^{65}\text{Zn}$ . There, for the first time, hybrid active pixel detectors were used. It was shown that  $P_{KK}$  can be obtained rather precisely, even with scarce energy information, by understanding and subtracting processes with similar experimental signatures. This work also demonstrates how pixel detectors can be applied to detect the hypersatellite-satellite photons in coincidence as a base for the (two-photon) angular correlation function.

Until the present, however, an uncorrelated emission has always been assumed in the investigation of hollow atoms in electron capture decays. By measuring the angular correlation functions, valuable information about shell structure and, especially, transition probabilities in many-electron atoms and ions can be obtained. These probabilities are known to be sensitive to the details of electron-electron and electron-photon interactions as well as to the relativistic corrections [9]. In this work, the first measurement of the angular correlation function is presented. Additionally, due to improved statistics and better understanding of the setup, the precision compared to our previous measurement of  $P_{KK}$  [8] was further improved.

\*benedikt.bergmann@utef.cvut.cz

## II. DESCRIPTION OF EXPERIMENT AND SIMULATION

Two Timepix detectors (further referred to as detectors A and B) were employed to record the x rays emitted from an  $^{55}\text{Fe}$  source. These detectors, which consist of an active silicon sensor layer that is segmented into pixels, faced each other with the radioactive  $^{55}\text{Fe}$  source in between. The detector technology is described in Sec. II B.

A mechanical PVC (polyvinyl chloride) support structure kept the detectors and the  $^{55}\text{Fe}$  source at fixed positions with the sensor layer normal in the horizontal plane of the laboratory. To reduce the number of registered shake-off electrons, two  $(50.7 \pm 1.4) \mu\text{m}$  thick Kapton foils were inserted between source and sensor layers. Details of the experimental setup are explained in [8].

### A. Radioactive source

As the angular resolution depends on the extension of the radioactive source, a dedicated  $^{55}\text{Fe}$  source with a very small diameter was produced by the German Metrology Institute PTB (Physikalisch Technische Bundesanstalt). In the production of the source a solution with  $^{55}\text{Fe}$  ions was deposited as a circular spot with approximately 1 mm diameter on top of a polyethylene foil. After drying, the source was sealed with a second thin polyethylene foil. The two  $(14.70 \pm 0.25) \mu\text{m}$  thick polyethylene foils were spanned in a ring-shaped aluminum support structure with 30 mm outer radius, 20 mm inner radius, and 3 mm thickness. The certified activity of the source was  $A_0 = (74.0 \pm 2.5) \text{ kBq}$  at 0:00 CET on January 1, 2013. A  $\gamma$  spectroscopy measurement detected a contamination with  $^{60}\text{Co}$  of  $A(^{60}\text{Co}) = (1.73 \pm 0.18) \text{ Bq}$ .

The  $^{55}\text{Fe}$  ground state nucleus  $(3/2)^-$  undergoes electron capture to the  $(5/2)^-$  ground state nucleus of  $^{55}\text{Mn}$  with a half-life of  $T_{1/2} = 2.747(8)$  years and with a  $Q$  value of 231.21(18) keV. A second forbidden decay to the excited  $(7/2)^-$  state of  $^{55}\text{Mn}$  occurs with a probability of  $1.3 \times 10^{-7}\%$ . The relaxation of the excited  $^{55}\text{Mn}$  nucleus proceeds via photon emission at 126.0(1) keV [10]. While the (relative) probability for a  $K$ -shell capture is  $P_K = 88.53(16)\%$ , an electron from the  $L$  shell is captured with  $P_L = 9.83(13)\%$  and an electron from the  $M$  shell with  $P_M = 1.63(8)\%$ , respectively.

The decay of the vacancies after electron capture occurs with the emission of the characteristic x-ray fluorescence lines of  $^{55}\text{Mn}$ . Given the detectors' discriminator threshold at about 3 keV, only  $K$  lines with the energies 5.88765 keV ( $K\alpha_1$ ), 5.89875 keV ( $K\alpha_2$ ), 6.49045 keV ( $K\beta_3$ ), and 6.5352 keV ( $K\beta_5$ ) can be detected. With the fluorescence yield  $\omega_K = 0.321$ , the probability of  $K$ -line photon emission per decay is  $P_K \times \omega_K = 28.42\%$  (see [11]).

To understand the contribution of the  $^{60}\text{Co}$  contamination in the source to the angular correlation function and the  $P_{KK}$  measurement, we will discuss the decay scheme of  $^{60}\text{Co}$  in the following.

$^{60}\text{Co}$  disintegrates by  $\beta$  decay to the excited levels of  $^{60}\text{Ni}$  with half-life 5.2711(8) years and  $Q$  value 2823.07(21) keV. In 99.88(3)% of the decays, the endpoint energy of the  $\beta$  spectrum is 317.32(21) keV. The second forbidden transition leads to endpoint energies of 664.46(21) keV (0.002%) and 1490.56(21) keV (0.12%), respectively. The deexcitation of

the  $^{60}\text{Ni}$  daughter nucleus proceeds by a cascade of  $\gamma$  rays. The most probable case is the emission of two  $\gamma$ 's with energies 1173.240(4) keV (99.85%) and 1332.508(4) keV (99.9988%) [11,12]. The lifetime of the intermediate state, which is 0.9 ps, is far below the time resolution of the Timepix detectors.

The angular correlation function of the two  $\gamma$ 's in this quadrupole-quadrupole transition reads  $W(\theta) = 1 + 1/8 \times \cos^2(\theta) + 1/24 \times \cos^4(\theta)$  [12]. No angular correlation exists between the emitted  $\beta$  and the  $\gamma$ 's [13]. For our analysis, the contribution of the  $^{60}\text{Co}$  contamination to the signal was determined with a Monte Carlo simulation. Due to the low detection efficiency for high-energy  $\gamma$ 's, their different signatures, and the small activity in the source compared to  $^{55}\text{Fe}$ , the  $^{60}\text{Co}$  contribution was found to be negligible (see below).

### B. Timepix pixel detectors

The Timepix detectors used in this work consist of 300  $\mu\text{m}$  thick p-on-n sensor layers. The sensor layers are flip-chip bump-bonded to a read-out ASIC (application-specific integrated circuit), which was developed within the Medipix Collaboration [14]. The ASIC pixelates the  $1.4 \times 1.4 \text{ cm}^2$  sensor area to a square matrix of 256 by 256 pixels with a pixel-to-pixel distance of 55  $\mu\text{m}$ .

A potential difference of 100 V between the unpixelated common anode and the pixelated cathode was applied to fully deplete the silicon diodes (pixels). For the data acquisition, the FITPIX interface was used together with the PIXELMAN software [15,16]. Both, the interface and the software, were developed by the Institute of Experimental and Applied Physics, Czech Technical University in Prague.

Ionizing radiation interacting in the silicon sensor layer creates free charge carriers. Before these charge carriers are collected at the corresponding pixel electrode, they induce mirror charges at the pixel electrodes, as they are drifting in the electric field. In each pixel cell, the induced current is converted to a voltage pulse by a charge-sensitive amplifier and compared to the globally adjustable discriminator threshold.

These thresholds were calibrated to energy by using the  $K$ -fluorescence lines from Mn, the  $L$  line from Pb, and the  $K$  lines from Sn. During calibration, the discriminator threshold is set well above the energy of the corresponding fluorescence line and continuously lowered. The number of registered hits is measured for each step. When the threshold reaches the energy of the fluorescence line, an increase of counts is observed, so that an edge in the threshold spectrum is pronounced. The threshold levels at the edges are assigned to the fluorescence energies. A linear extrapolation to the set threshold gives minimal usable discriminator thresholds at  $(3.15 \pm 0.10) \text{ keV}$  (detector A) and  $(3.26 \pm 0.33) \text{ keV}$  (detector B).

Depending on each pixel's mode of signal processing operation, the voltage pulse from the charge sensitive amplifier can be used in different ways. In time-of-arrival (ToA) mode, which was exclusively used in this work, a reference clock measures the time from the moment when the pulse crosses the threshold until the acquisition is terminated by a shutter signal.

Due to repulsion and diffusion of the charge carriers and due to extended track lengths of the ionizing primary particles,

the charge is spread out among neighboring pixels, leading to clusters of triggered pixels. Using pattern recognition, different cluster shapes can be identified and categorized. The shapes indicate energy deposition and particle type [17]. The x rays and low energy electrons in this work are detected as small clusters with one or two triggered pixels.

The detectors were synchronized by dedicated Nuclear Instrumentation Module (NIM) electronics, which provided a trigger signal that started and stopped the acquisition after the selected exposure time. Thus, similarly to a camera, pictures (called frames) of ionizing radiation were recorded. The clock frequency of 9.6 MHz was chosen, giving a time resolution of 104.2 ns per time bin. As each pixel cell is equipped with a 14-bit pseudorandom counter, the longest period that can be stored in each pixel is 11 810 clock cycles, restricting the acquisition time for each frame to 1.2 ms.

The acquisition is followed by the read-out, in which the content of the counters of each pixel is retrieved and sent to the control computer. During this process the detectors are not capable of recording further events. Once both detectors have finished the data transfer, a new trigger signal is sent. A framerate of 32 Hz was achieved.

### C. Detector simulation

All simulations in this work were carried out with the Monte Carlo package ROSI (Roentgen Simulation package) [18]. It is based on EGS4 (Electron Gamma Shower) and its low energy photon scattering expansion LSCAT. The simulation included Fano noise [19], charge carrier transport (according to the model of Spieler and Haller [20]), and induction in the pixel electrodes (using the Ramo-Shockley theorem [21,22]). The

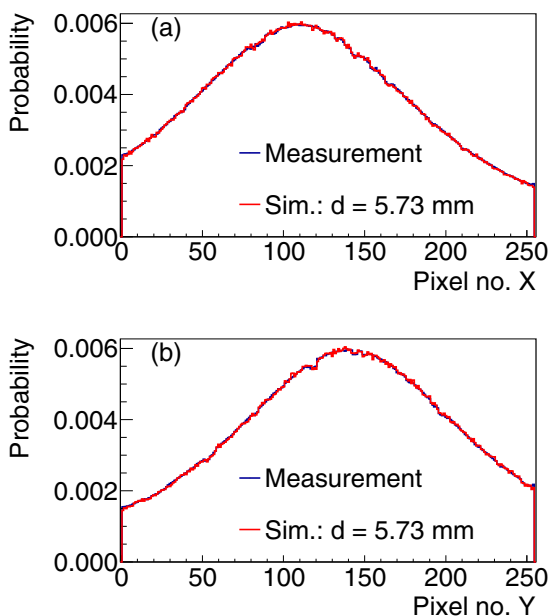


FIG. 1. Detector A: Comparison of the simulated and measured projections on the axes of the detectors after the removal of pixels with higher noise level and the removal of hits with contact to defect and noisy pixels. The excellent agreement confirms the proper modeling of the distances and source position in the simulation.

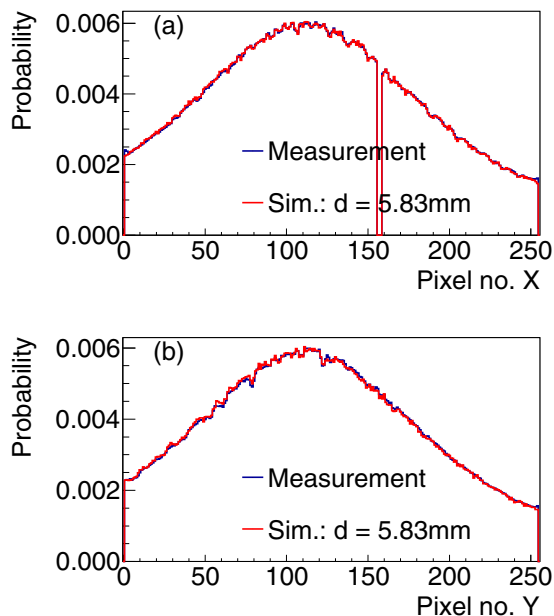


FIG. 2. Same as Fig. 1 but for detector B. A dead column can be seen by a missing entry in the distribution of  $x$  coordinates. This was taken into account in the simulation.

analog noise of the amplifier and the discriminator threshold levels were modeled by a Gaussian distribution with a standard deviation of 396 eV. The accuracy and reliability of the simulation were verified by Sievers *et al.* [23].

The setup is modeled in detail in the Monte Carlo simulations: it includes the PVC holder, the aluminum ring, the polyethylene source sealing, the Kapton foils, and the detectors. The detectors were modeled as a layer structure with the FR4 (flame retardant) printed circuit board (PCB), the under-bump metallization on the ASIC side, a layer with the  $256 \times 256$  spherical bump bonds, the under-bump metallization on the sensor side and the  $300 \mu\text{m}$  thick active silicon layer. Particles were emitted from a cylindrical source spot. The lateral displacements of the detectors and the radius of the source were determined with high precision by adjusting these quantities in the simulation to obtain the detector responses in the form of the projections of counts on the pixel matrix axes as measured. A dead column, a column which cannot be read out, was present in detector B, and taken into account in the simulation by omitting pixels with the corresponding column number. We have simulated a source radius of 0.5 mm, a distance of 5.73 mm from detector A, and a distance of 5.83 mm from detector B. As demonstrated in Figs. 1 and 2, an excellent agreement between measurement and simulation was achieved.

## III. DATA EVALUATION TECHNIQUES

### A. Measurement principles

In the following section we describe the calculations carried out to estimate the contribution of background processes to the coincident peak. In particular, we discuss separately the processes resulting in a doubly ionized  $K$  shell, which are

TABLE I. Overview of the contributions of each process to the prompt peak.

Process	Contribution to the signal (%)
HS-S	94.44
S- <i>KK</i> (HS missed or Auger emission)	1.30
HS- <i>KK</i> (S missed or Auger emission)	0.97
IB- <i>K</i>	2.35
<i>KLLK</i> -S	0.58
External background	0.39
Cobalt impurity	$6.5 \times 10^{-5}$

the  $P_{KK}$  signal, and processes leaving the atom in a one-hole state or that do not create vacancies at all in Secs. III A 1 and III A 2, respectively. Their contributions to the prompt peak are summarized in Table I.

We keep the discussion and nomenclature close to our previous publication [8]. Likewise, the simulated particle detection yields  $\delta$  are defined as the probability that a particle emitted in the source is detected with the correct signature (a cluster with a maximum of two pixels). The detection yields were simulated for the new diameter of the  $^{55}\text{Fe}$  source and changes of geometry due to dismounting the old and mounting the new source in the holder.

For the further discussion we introduce the term “hit” when we refer to a particle registered with the correct signature in one of the detectors. We define an “event” as the detection of two hits within the coincidence window.

### 1. Coincident events after double vacancy creation

In the creation and relaxation of a double  $K$ -shell vacancy, at most three detectable particles can be emitted. These are the shake-off electron with energies up to 218 keV [24], indicated with subscript  $KK$  (for  $K$  capture and  $K$  shake-off), the hypersatellite (HS) and the satellite photon (S). The energies of ejected  $K$  electrons were chosen according to the measured spectrum by Pengra *et al.* [24]. Auger electrons are not detectable as they are completely absorbed in the polyethylene foils of the source container or in the additional Kapton foils. The following five combinations of events can be found.

- (i) Most likely is the detection of the hypersatellite-satellite (HS-S) cascade but without the shake-off electron. The number of these events is given by

$$\begin{aligned} N_{\text{HS-S}} &= \omega_S P_K A(t) t_{\text{meas}} \omega_H P_{KK} \delta_{\text{HS}} \delta_S (1 - \delta_{KK}) \\ &= N_K \frac{\omega_H \omega_S}{\omega_K} P_{KK} \frac{\delta_{\text{HS}} \delta_S}{\delta_K} (1 - \delta_{KK}). \end{aligned} \quad (1)$$

$\omega_K = 0.321$  is the fluorescence yield for the filling of the single- $K$ -hole state,  $P_{KK}$  is the probability for double  $K$ -shell ionization, and  $N_K = \delta_K \omega_K P_K A(t) t_{\text{meas}}$  is the total number of detected fluorescence photons in the measurement time  $t_{\text{meas}}$ .  $\omega_H = 0.344 \pm 0.007$  is the fluorescence yield for the filling of one of the two  $K$ -shell vacancies in the double- $K$ -hole state, associated with the hypersatellite emission.  $\omega_H$  was obtained by a logarithmic interpolation of the data

given in Table V in the work of Chen [25]. We assumed a systematic uncertainty of 2%.  $\omega_S = 0.339 \pm 0.007$  is the fluorescence yield for the filling of a “spectator” vacancy in the  $L$  shell. We obtained  $\omega_S$  by evaluating a second-order polynomial fit to the  $\frac{\omega_S}{\omega_K}$  curve given in Fig. 3 of [26] at  $Z = 25$ . Again, we assumed a systematic uncertainty of 2%.

- (ii) Coincident detection of the hypersatellite photon with the electron that is *shaken* into the continuum, missing the satellite photon:

$$N_{\text{HS-}KK} = N_K \frac{\omega_H \omega_S}{\omega_K} P_{KK} \frac{\delta_{\text{HS}} \delta_{KK}}{\delta_K} (1 - \delta_S). \quad (2)$$

- (iii) Similarly, the coincident detection of the satellite photon with the shake-off electron, missing the hypersatellite photon:

$$N_{\text{S-}KK} = N_K \frac{\omega_H \omega_S}{\omega_K} P_{KK} \frac{\delta_S \delta_{KK}}{\delta_K} (1 - \delta_{\text{HS}}). \quad (3)$$

- (iv) The coincident detection of the satellite with the shake-off electron, while the first vacancy in the  $K$  shell is filled with the simultaneous emission of an Auger electron:

$$N_{\text{S-}KK, \text{Auger}} = N_K \frac{\omega_S}{\omega_K} (1 - \omega_H) P_{KK} \frac{\delta_S \delta_{KK}}{\delta_K}. \quad (4)$$

- (v) The coincident detection of the hypersatellite photon together with the shake-off electron, while the second  $K$ -shell vacancy filling proceeds through Auger electron emission:

$$N_{\text{HS-}KK, \text{Auger}} = N_K \frac{\omega_H}{\omega_K} (1 - \omega_S) P_{KK} \frac{\delta_{\text{HS}} \delta_{KK}}{\delta_K}. \quad (5)$$

For the determination of  $P_{KK}$  all these combinations were considered as part of the signal. For the angular correlation measurement, only  $N_{\text{HS-S}}$  is of interest, which is, due to the design of the setup, by far the dominant contribution.

### 2. Coincident events from background processes

There are a number of further processes that may lead to detected “events” but which are not related to an empty  $K$  shell. These are addressed in the following.

- (i) Dominating are the accidental coincidences, i.e., two  $K$ -line photons registered within the coincidence window. Their number  $N_{\text{acc}}$  was determined with high precision in the evaluation process and subtracted.
- (ii) Internal bremsstrahlung photons can mimic an event when detected together with a  $K$ -line photon from the  $K$ -shell vacancy filling. Due to the motion of the captured electron in the Coulomb field of the nucleus, internal bremsstrahlung (IB) photons with energies up to 231.21 keV can be emitted [27]. The probability of this second-order process is  $P_{\text{IB}} = 2.5808 \times 10^{-5}$  (see [8] and discussion therein). The number of internal bremsstrahlung  $K$ -line photon coincidences amounts to

$$N_{\text{IB-}K} = N_K P_{\text{IB}} \delta_{\text{IB}}. \quad (6)$$

- (iii)  $L$ -electron capture succeeded by  $K$  shake-off ( $LK$ ) and  $K$ -electron capture followed by  $L$  shake-off ( $KL$ ) leave the atom with vacancies in the  $K$  and in the  $L$  shells. The final states of both cases cannot be distinguished. Filling the vacancies can proceed through a satellite and an  $L$ -line photon. Whereas an  $L$ -line photon has an energy too small to be detected, the satellite photon can be registered together with the shake-off electron. This contributes with

$$N_{S-KLLK} = N_K P_{KLLK} \delta_{KLLK} \quad (7)$$

to  $N_{\text{peak}}$ , with  $P_{KLLK} = 3.161 \times 10^{-4}$  [28].  $M$ - and higher-shell contributions are negligible [8].

- (vi) Related to the  $\beta$  decay of the  $^{60}\text{Co}$  impurity, three coincident particles are emitted, i.e., the electron with an energy up to 317.32(21) keV and two  $\gamma$  rays of energies 1173.240(4) keV and 1332.508(4) keV from the relaxation of the excited  $^{60}\text{Ni}$  daughter nucleus. Three combinations were found to be able to create events. The electron, that is detected in coincidence with one of the  $\gamma$  rays, missing the second  $\gamma$  ray, and the electron being missed, whereby the two  $\gamma$  rays are detected in coincidence. We can thus describe the number of registered  $^{60}\text{Co}$  coincidences by

$$\begin{aligned} N_{\text{Co}} = & A_{\text{Co}}(t) t_{\text{meas}} \times [\delta_{\text{Co},e} \delta_{\text{Co},\gamma 1} (1 - \delta_{\text{Co},\gamma 2}) \\ & + \delta_{\text{Co},e} \delta_{\text{Co},\gamma 1} (1 - \delta_{\text{Co},\gamma 2}) \\ & + \delta_{\text{Co},\gamma 1} \delta_{\text{Co},\gamma 2} (1 - \delta_{\text{Co},e})]. \end{aligned} \quad (8)$$

The number of  $^{60}\text{Co}$  disintegrations  $N_{\text{Co,emitted}}(t) = A_{\text{Co}}(t) t_{\text{meas}}$  for the duration of the measurement was calculated separately for each 1.7-days-long data-taking run and summed. With a proportion of only  $6.5 \times 10^{-5}\%$  of events in the coincidence peak, this contribution could be neglected.

- (v) Compton scattered x rays and  $\gamma$ 's as well as interrupted muon tracks from the natural radioactive background can also mimic the signal. Their number was estimated in a measurement without radioactive material in the source container. By excluding small angles, their contribution was reduced significantly from further analysis (see Sec. III B 3). For the  $P_{KK}$  determination, the number of remaining events was scaled according to the measurement times and subtracted. To the angular distribution, a contribution of less than 1% was found.

To account for the angular correlation of the HS-S coincidence and the two- $\gamma$  coincidence of the  $^{60}\text{Ni}$  relaxation, the two-particle yields  $\delta_{\text{HS-S}}$  and  $\delta_{\text{Co},\gamma 1-\text{Co},\gamma 2}$  are defined, and they replace the products  $\delta_{\text{HS}} \delta_{\text{S}}$  and  $\delta_{\text{Co},\gamma 1} \delta_{\text{Co},\gamma 2}$  in Eqs. (1) and (8), respectively. In the simulation, two particles are emitted from the same origin within the source spot with the corresponding angular relation. An event is counted when two hits are registered.

Using  $P_{KK} = (1.388 \pm 0.037) \times 10^{-4}$  as given in Sec. IV and the simulated yields (see Table II), the contribution of each process to the number of events in the peak  $N_{\text{peak}}$  (the signal) is calculated. Table I gives a summary of the obtained values.

TABLE II. Quantities that were used in the calculation of  $P_{KK}$  with their statistical ( $1\sigma$ ) and systematic uncertainties  $(\Delta x)_{\text{sys}}$ . The third column indicates how the value was determined.

Quantity	Value	$\sigma(x)$	$(\Delta x)_{\text{sys}}$	Source
$\delta_K(\text{meas.})$	0.290	$2.1 \times 10^{-11}$	$\pm 5.0 \times 10^{-7}$	exp.
$\delta_K(\text{sim.})$	0.282		+0.018 -0.016	sim.
$\delta_{\text{HS}}$	0.304		+0.016 -0.014	sim.
$\delta_{\text{S}}$	0.293		+0.018 -0.015	sim.
$\delta_{KK}$	0.00149		+0.00012 -0.00009	sim.
$\delta_{\text{IB}}$	0.0154		+0.00029 -0.00062	sim.
$\delta_{KLLK}$	0.000308		+0.000024 -0.000023	sim.
$\kappa_{\text{HS}}$	1.0769		+0.019 -0.011	sim.
$\kappa_{\text{S}}$	1.0376		+0.0138 -0.0068	sim.
$\gamma_{\text{HS-S}}$	0.974			sim.
$\gamma_{\text{HS-KK}}$	0.961			sim.
$\gamma_{\text{S-KK}}$	0.962			sim.
$\gamma_{\text{IB-K}}$	0.963			sim.
$\gamma_{\text{S-KLLK}}$	0.951			sim.
$\alpha_{\text{cor.}}$	1.017			sim.
$N_K$	4 205 878 386	64 853		exp.
$N_{\text{prompt}}$	2 776 240	1 666		exp.
$N_{\text{acc.}}$	2 710 909	225		exp.
$N_{\text{peak}}$	65 331	1 681		exp.
$N_{\text{BG,ext.}}$	279	37		exp.
$P_{\text{loss}}^{\text{fine}}$	0.0919			calc.
$A_0$ (kBq)	74.0		$\pm 2.5$	meas.
$\omega_{\text{H}}$	0.344		$\pm 0.007$	[25]
$\omega_{\text{S}}$	0.339		$\pm 0.007$	[26]
$P_{KLLK}$	$3.161 \times 10^{-4}$		$\pm 0.316 \times 10^{-4}$	[28]
$P_{\text{IB}}$	$2.58 \times 10^{-5}$		$\pm 0.04 \times 10^{-5}$	[8]

## B. Data analysis

### 1. Data acquisition and processing

The data were taken in runs with a duration of 1.7 days each. After each run the data were compressed and sent to the data analysis server. 872 752 188 frames (data acquisitions of 1.2 ms length) were recorded with the  $^{55}\text{Fe}$  source and 178 367 467 without the radioactive material. The ToA mode of the Timepix with a clock frequency of 9.6 MHz was used. In each frame individual clusters (groups of adjacent pixels) were identified. The timestamp of the hit was defined as the highest counter value within one cluster. Hits seen as clusters with more than two pixels, hits directly at the beginning (with counter values bigger than 10 000), and hits at the end of each frame (with counter value 1) are excluded from further analysis. The effective lifetime of the measurement was 10.5 days for the measurement with the radioactive source and 2.2 days for the measurement without the source.

Pixels showing a significantly higher count rate (noisy pixels) and pixels not measuring at all (dead pixels) were identified in the measurement without the source. Hits with contact to excluded pixels or to the edges of the sensor layer were omitted. The sensitive area was thus artificially reduced by 1335 pixels (2%) (detector A) and 2551 pixels (3.9%) (detector B). In total, with the source  $N_K = 4 205 878 386$

one- or two-pixel clusters were recorded.  $N_{K,BG} = 8482$  were measured without the source.

For the coincidence analysis, the frames were divided into 50 equally long time-slices, of which only time-slices containing exactly two hits were further processed. A common coordinate system for both detectors was chosen, where the center of the source was defined as the origin. For two-pixel clusters, the  $x$  and  $y$  positions were given by the pixel with the earlier time response (higher counter value).

The momentum vectors  $\vec{p}_1$  and  $\vec{p}_2$  were calculated assuming the particles propagated from the center of the source. The angle  $\theta$  between the momenta—named emission angle in the following—is thus given by

$$\theta = \arccos\left(\frac{|\vec{p}_1 \vec{p}_2|}{|\vec{p}_1| |\vec{p}_2|}\right). \quad (9)$$

The time difference of the two hits, the angle, and the involved detectors are stored.

## 2. Simulated angle resolving power and angular acceptance

Radial extension of the source, photons scattering at the atoms of the inserted Kapton foils, and the dimensions of the pixels induce an uncertainty on the angle reconstruction. The uncertainty analysis was performed with a Monte Carlo simulation. In this simulation, two photons are emitted simultaneously. The angles between the two photons are sampled in a way so that the flux on the surface of a sphere centered at the source origin is homogenous. The directions of emissions are uncorrelated. The emission angle is chosen for each of the two photons independently. The two photons start at the same location in the source, which is uniformly distributed over the radioactive source spot. The same analysis as for the measured data is performed on the simulated data.

The linearity of the reconstruction method is demonstrated by the scatter plot of the reconstructed versus the true emission angle in Fig. 3. A correlation factor of 0.9911 was found. Entries far away from the straight line through the origin are due to scattering of the photons. The width of the correlated area indicates the error due to the extension of the radioactive source and the pixel dimension.

In order to understand systematic uncertainties of the setup, we have investigated the detection efficiency of a given emission angle. We have defined the angular acceptance as the

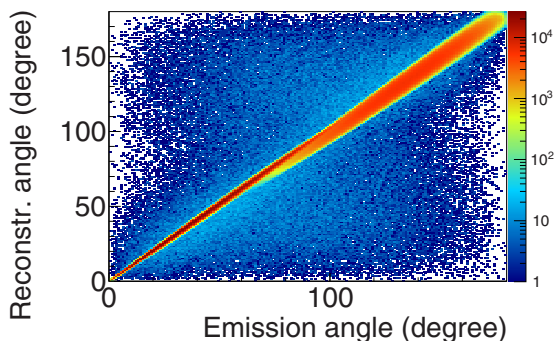


FIG. 3. Simulation: scatter plot of the angle, reconstructed in the analysis, versus the true emission angle.

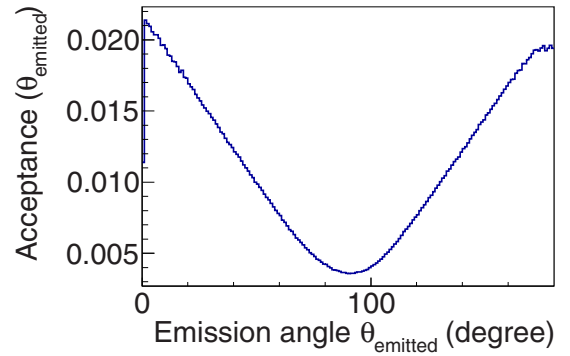


FIG. 4. Simulated angular acceptance as a function of the emission angle. Small-angle emission and back-to-back emission have a higher probability of being registered by the measurement setup.

probability to count an emission angle as an event after all cuts were applied. In Fig. 4 this angular acceptance is shown as a function of the emission angle. The acceptance is not constant for all emission angles; i.e., due to the design of the setup, some emission angles are favored. We find a ratio of the maximal acceptance (for back-to-back emission and for small angle emission) to the minimal acceptance (at about 90° emission angle) of approximately 4.

## 3. Measurement without the source

182 events were found in the coincidence window of 104.2 ns in the measurement without the source. The angular distribution of these coincident events peaks towards small angle emission (see the blue curve in Fig. 5). Unfortunately, the rate of coincidences from external radioactive background is not very stable in time. This made it difficult to predict their contribution to the events of the coincident peak by scaling measuring times. Therefore, reliable angular correlation functions could only be obtained for angles above 12°. Requiring a minimum angle of 12° reduced the events from external background by 59.3% to 74 events (red curve in Fig. 5). The same cut was used in the determination of  $P_{KK}$ ,

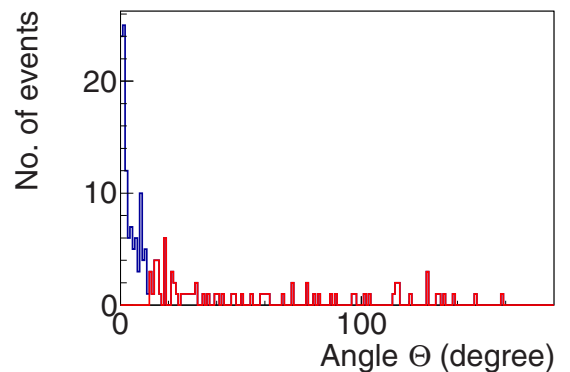


FIG. 5. Angular distribution of events from the measurement of the external (natural) radioactive background. 182 events were found in the coincidence window (blue and red curves). By requiring a minimum angle of 12°, only 74 events remain (red curve).

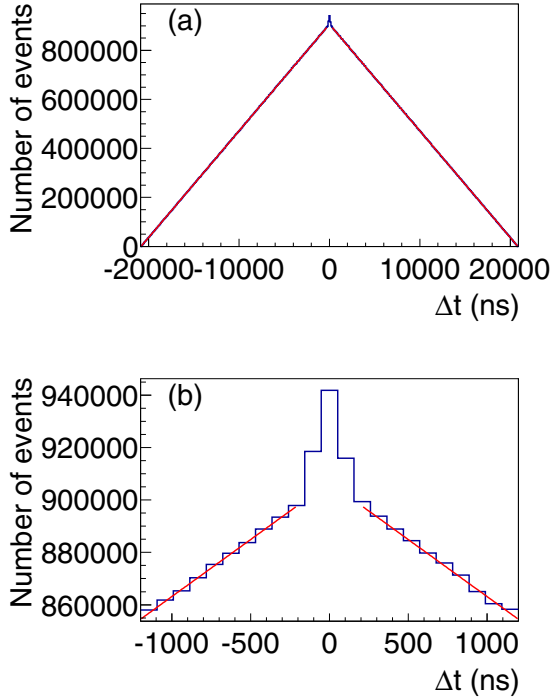


FIG. 6. Distribution of the time differences for time-slices with exactly two hits. In (a) the full spectrum is shown, in (b) a zoom of the region of interest with the prompt peak. The triangular shape of the accidental coincidences is due to the subtraction of two uniform random variables.

reducing the signal by only 2.5% (estimated in the simulation by interpolating the measured angular distribution according to the fit shown below).

#### 4. Spectrum of time differences

The spectrum of the time differences of the events from the measurement with the radioactive source in doubly hit time-slices is shown in Fig. 6. A prompt peak sits on top of the triangle caused by accidental coincidences. The possibility of detecting a photon is uniform in the time of detection values of the time-slices. Therefore, the probability to accidentally detect an event is described by a convolution of two uniform distributions. To determine the number of accidental coincidences in the prompt peak, the following function was adapted to the measured spectrum (see Fig. 6):

$$N(\Delta t) = N_0 - \alpha|\Delta t| \quad \text{for } 104.2 \text{ ns} < |\Delta t| \leq t_{\text{slice,max}}. \quad (10)$$

Extrapolating into the coincidence region ( $|\Delta t| \leq 104.2 \text{ ns}$ ) results in  $N_{\text{prompt}} = 2776240$  events, of which  $N_{\text{acc.}} = 2710909 \pm 225$  were accidental coincidences. The prompt peak consists of  $N_{\text{peak}} = 65331 \pm 1681$  events.

#### 5. Determination of the angular correlation function

In this analysis, three classes of events are treated separately. The first is the detection of two hits in detector A,

while detector B does not register any particle. The second is the corresponding case, with detector B having two hits and detector A not being triggered. These two categories are most likely for emission of both photons into the same hemisphere. The third case is the detection of exactly one hit in detector A and exactly one in detector B. Back-to-back emission would fall into this category. In [8] the same classification was used to indicate that there was no asymmetry in forward and backward emission by showing that the calculated  $P_{KK}$  for the different classes agreed within their error intervals.

By cutting on timestamps ( $|\Delta t| \leq 104.2 \text{ ns}$ ), the angular distribution  $f_{\text{prompt}}(\theta)$  of prompt events was obtained. This distribution contains accidental and real coincidences. This can be expressed as

$$f_{\text{prompt}}(\theta) = f_{\text{acc.}}(\theta) + f_{\text{real}}(\theta). \quad (11)$$

Events outside the coincident region ( $|\Delta t| > 104.2 \text{ ns}$ ) were used to determine  $f_{\text{acc.}}(\theta)$ . Due to the huge amount of random coincidences,  $f_{\text{acc.}}(\theta)$  is automatically measured very precisely. From Eq. (11), we find the angular distribution of the true coincidences by subtracting the angular distribution of the random events scaled according to their contribution to the coincidence region:

$$f_{\text{real}}(\theta) = f_{\text{prompt}}(\theta) - \frac{N_{\text{acc.}}}{N_{\text{prompt}}} f_{\text{acc.}}(\theta). \quad (12)$$

This was carried out separately for the three categories defined above, as the amount of random coincidences differs among the classes (due to the different distances of the detectors from the source), and as the angular acceptances for classes 1 and 2 overlap with the one of class 3.

To correct for the limited solid angle of the detectors, the Monte Carlo simulation described above was carried out for uncorrelated emission of the hypersatellite-satellite (HS-S) photons. Both photons start at the same location, homogeneously distributed within the source spot. The simulated data were treated in the same way as the measured data determining the angular response function of the signal to uncorrelated emission:  $R_{\text{HS-S}}^{\text{uncorr.}}(\theta)$ .

A similar simulation was carried out if the two photons are assumed to emerge from different locations in the source spot. This simulated the angular response function of accidental coincidences  $R_{\text{acc.}}^{\text{uncorr.}}(\theta)$ . The measured angular correlation functions  $W_{\text{HS-S}}(\theta)$  and  $W_{\text{acc.}}(\theta)$ , characterizing the deviation from uncorrelated emission, are then defined as

$$W_{\text{HS-S}}(\theta) = \frac{f_{\text{real}}(\theta)}{R_{\text{HS-S}}^{\text{uncorr.}}(\theta)} \quad (13)$$

and

$$W_{\text{acc.}}(\theta) = \frac{f_{\text{acc.}}(\theta)}{R_{\text{acc.}}^{\text{uncorr.}}(\theta)}. \quad (14)$$

$W_{\text{acc.}}(\theta)$  is shown in Fig. 7. As expected,  $W_{\text{acc.}}(\theta)$  is consistent with a uniform distribution around the value 1. Deviations of less than 0.5% demonstrate the excellent accuracy of the description of the setup in the simulation and indicate a small systematic error.

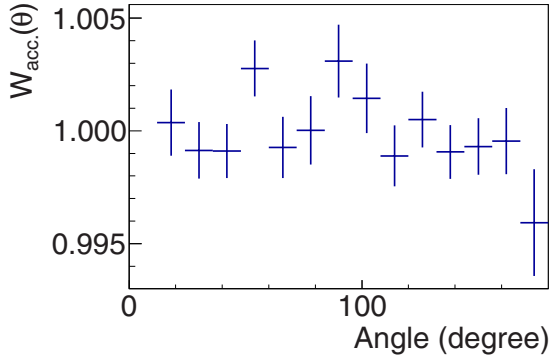


FIG. 7. Angular correlation function  $W_{\text{acc.}}(\theta)$  for uncorrelated emission, as given by accidental coincidences. Deviations of less than 0.5% from uniformity demonstrate the excellent accuracy of the description of the setup and detector responses in the simulation and indicate the systematic uncertainty of the measurement.

### 6. Calculation of $P_{KK}$

In our previous work [8], it was shown that by selectively simulating the energy dependence of the photon yields, the

$$P_{KK} = \frac{\frac{N_{\text{prompt}} - N_{\text{acc.}}}{1 - P_{\text{loss}}} - N_{\text{BG,ext.}} - N_K(P_{\text{IB}}\delta_{\text{IB}}\gamma_{\text{IB-K}} + P_{KLLK}\kappa_S\delta_{KLLK}\gamma_{S-KLLK})}{N_K \frac{\omega_{\text{H}}\omega_{\text{S}}}{\omega_K} [\alpha_{\text{cor.}}\gamma_{\text{HS-S}}\kappa_{\text{HS}}\kappa_S\delta_K(1 - \delta_{KK}) + \gamma_{S-KK}\kappa_S\delta_{KK}(\frac{1}{\omega_{\text{H}}} - \kappa_{\text{HS}}\delta_K) + \gamma_{\text{HS-KK}}\kappa_{\text{HS}}\delta_{KK}(\frac{1}{\omega_{\text{S}}} - \kappa_S\delta_K)]}. \quad (16)$$

$\alpha_{\text{cor.}} = \frac{\delta_{\text{HS-S}}^{\text{cor.}}}{\delta_{\text{HS}}\delta_{\text{S}}} = 1.017$  corrects for the deviation of the angular correlation function from uncorrelated emission. The angles were sampled according to the fit to the angular correlation function as shown in Fig. 8.

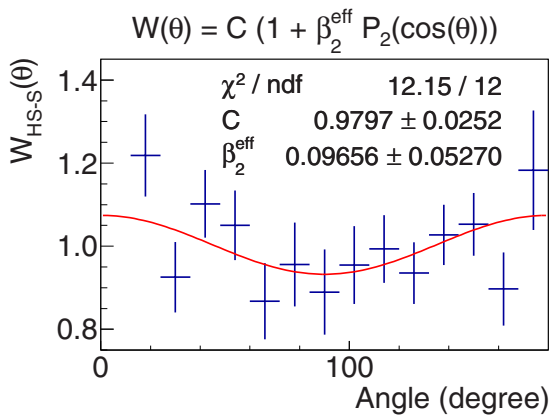


FIG. 8. Measured angular correlation function. Note the different ranges on the ordinate compared to Fig. 7. Fitting  $W(\theta) = C[1 + \beta_2^{\text{eff}} P_2(\cos\theta)]$  to the experimental data an “effective” anisotropy parameter  $\beta_2^{\text{eff}}(\text{exp}) = 0.09656 \pm 0.05270$  was obtained. The interpretation and the comparison to theoretical predictions are discussed in the text.

systematic error of  $P_{KK}$  could be reduced. Therefore, in the simulation, we introduced the following dimensionless factors:

$$\kappa_i = \frac{\delta_i}{\delta_K} \quad \text{with } i \in \text{HS,S}. \quad (15)$$

Due to the strength of the source and the long measurement time,  $\delta_K(\text{meas.}) = 0.290$  was determined with negligible errors. The agreement of the measured with the simulated detection yield  $\delta_K(\text{sim.}) = 0.282_{-0.016}^{+0.018}$  demonstrates once again the reliability of the simulation.

By selecting only time-slices with exactly two hits, events accidentally falling into the same time-slice with one or more  $K$ -line photons were lost. As the detection of photons in a given time interval is a purely statistical process, it follows a Poisson distribution. With the mean number of detected events per slice  $p = 0.0964$ , the probability to lose an event was given by  $P_{\text{loss}} = 1 - e^{-p} = 0.0919$ .

$\gamma_i$  was defined to account for the loss due to the cuts on the emission angle. It was estimated in the simulation separately for the possible combinations, taking the angular correlation into account.

With Eqs. (1)–(7), Eq. (16) in [8] was modified to

## IV. RESULTS AND DISCUSSION

### A. Angular correlation function

The correlation function of the hypersatellite-satellite cascade, as determined according to Eq. (13) is shown in Fig. 8.

In order to better understand the observed angular correlation  $W(\theta)$ , we explored theoretically the radiative decay of a double  $K$ -shell vacancy. In the first step of this study we focused on the correlation between photons emitted in a transition between two well-defined fine-structure levels:

$$\begin{aligned} |1s^{-2} : J_a\rangle &\rightarrow |1s^{-1}2p^{-1} : J_b\rangle + \gamma_{\text{HS}} \\ &\rightarrow |2p^{-2} : J_c\rangle + \gamma_{\text{HS}} + \gamma_{\text{S}}. \end{aligned} \quad (17)$$

Here  $J_a$ ,  $J_b$ , and  $J_c$  are the total angular momenta of initial, intermediate and final ionic states, respectively. Since the (inner-shell) hypersatellite transitions are very little affected by the valence electrons, we assume an initial  $1s^{-2}$  closed-shell configuration with  $J_a = 0$  for the (empty)  $K$ -shell state. With this assumption, the angular correlation between  $\gamma_{\text{HS}}$  and  $\gamma_{\text{S}}$  x rays is given by

$$W_{J_b J_c}(\theta) = 1 + \mathcal{A}_{20}(J_b) f_2(J_c, J_b) P_2(\cos\theta), \quad (18)$$

where the magnetic sublevel population of the intermediate state  $|1s^{-1}2p^{-1} : J_b\rangle$  after the emission of the hypersatellite photon is described by the alignment parameter [29]

$$\mathcal{A}_{20}(J_b) = \langle J_b 1 J_b - 1 | 20 \rangle \sqrt{2J_b + 1} \delta_{J_b 1}. \quad (19)$$

The angular correlation (18) depends, moreover, on the function  $f_2$  which reflects the electronic structure of the ion

and, within the leading electric-dipole order, reads as

$$f_2(J_c, J_b) = (-1)^{1+J_b+J_c} \sqrt{\frac{3(2J_c+1)}{2}} \begin{Bmatrix} 1 & 1 & 2 \\ J_c & J_c & J_b \end{Bmatrix}. \quad (20)$$

The electric dipole approximation (18)–(20) is well justified for the radiative transitions in low- and medium- $Z$  atoms, for which the contributions from the nondipole components of the radiation field are known to be negligible.

Equations (18)–(20) describe the angular correlation of photons emitted in the transitions (17) between well-defined fine-structure states. However, such individual fine-structure lines were not resolved in the present experiment. Due to the restricted resolution of the photon detectors, only the average (i.e., the proper superposition) of the allowed  $|1s^{-2} : J_a\rangle \rightarrow |1s^{-1}2p^{-1} : J_b\rangle \rightarrow |2p^{-2} : J_c\rangle$  transitions is observed. If we assume that the energy splitting between the fine-structure levels  $|J_a\rangle$ ,  $|J_b\rangle$ , and  $|J_c\rangle$  is larger than their natural widths, the angular correlation function for such a superposition can be obtained as

$$W(\theta) = \sum_{J_b J_c} N_{bc} [1 + A_{20}(J_b) f_2(J_c, J_b) P_2(\cos \theta)] \\ = 1 + \beta_2^{\text{eff}} P_2(\cos \theta). \quad (21)$$

Here, the weight factors  $N_{bc}$  describe the contribution of individual fine-structure transitions to the overall angular correlation. These factors can be estimated from the branching ratios for the radiative transitions, and are normalized as  $\sum_{J_b J_c} N_{bc} = 1$ .

We have employed the angular correlation function (21) in order to fit the experimental data for the decay of the double  $K$ -shell vacancy of the manganese atom. From this fitting, we determined the “effective” anisotropy parameter  $\beta_2^{\text{eff}}(\text{exp}) = 0.09656 \pm 0.05270$  which can be compared with the theoretical prediction  $\beta_2^{\text{eff}}(\text{theor}) = 0.09735$ . The theoretical result was obtained based on Eq. (21) where the weight factors were calculated within the framework of the multiconfiguration Dirac-Fock (MCDF) approach [30]. The close agreement between the experimental and theoretical data for the anisotropy  $\beta_2^{\text{eff}}$  confirms the assumption that the outer-shell electrons do not affect the angular properties of the hypersatellite and satellite emission (17).

## B. Double $K$ -shell vacancy production probability

With Eq. (16), with the values summarized in Table II, as well as a systematic error  $\Delta P_{KK, \text{sys}} = 0.042 \times 10^{-4}$ , we obtain

$$P_{KK} = (1.388 \pm 0.037) \times 10^{-4}. \quad (22)$$

In the error estimation, the statistical and systematic errors were treated separately. Systematic uncertainties arose due to the improper knowledge of the analog detector thresholds, Kapton foil thicknesses, distances of the detectors to the source, and the interpolation uncertainty of the double- $K$ -hole fluorescence yield. Their effects on the yields were estimated by varying the corresponding value in the simulation within

their error bands. The uncertainty of the source activity was taken into account in the calculation of the detection yield  $\delta_K(\text{meas.})$  by Gaussian error propagation.  $\delta_K(\text{meas.})$  and its error  $\Delta\delta_K(\text{meas.})$  were calculated separately for each run and averaged, weighted by the errors.

Numbers that were measured by pure counting of events, i.e., the number of fluorescences  $N_K$ , the number of events in the peak ( $N_{\text{prompt}} - N_{\text{acc.}}$ ), and the number of background events  $N_{\text{BG,ext.}}$  follow Poissonian statistics.

The statistical and systematic error assignment on  $P_{KK}$  was done by a Monte Carlo approach. For each quantity a set of random numbers were generated according to their distributions by calculating  $P_{KK}$  for all possible combinations. By this, the distribution  $P_{KK}$  around the mean value was obtained. The errors assigned to  $P_{KK}$  represent the 68.2% confidence intervals.

In order to compare our result with the result of Campbell *et al.* [7] on the same nucleus we adapt their value  $P_{KK} = (1.3 \pm 0.2) \times 10^{-4}$  to reflect the differing single and double  $K$ -shell vacancy fluorescence yields. For this, the ratio  $\frac{\omega_{\text{H}}}{\omega_K} = 1.07$  was used in this work (see the discussion in Sec. III A). In lack of measurements and calculations, Campbell *et al.* [7] had to assume  $\omega_K \approx \omega_{\text{H}}$ . For the comparison, we stay with the assumption that the fractional intensities of the  $K_\beta$  lines in the  $K$ -x-ray series do not differ between the filling of the single and the double  $K$ -shell vacancy states. With Eq. (10) in Campbell *et al.* [7], we obtain the adapted result:  $P_{KK} = (1.2 \pm 0.2) \times 10^{-4}$ . The result of Michel *et al.* [8] has to be modified to account for the higher fluorescence yields of the hypersatellite and the satellite lines. The result is  $P_{KK} = (1.358 \pm 0.070) \times 10^{-4}$ . With the fluorescence yields’ interpolation uncertainties of 2%, the systematical uncertainty increases to  $0.062 \times 10^{-4}$ . The experimental  $P_{KK}$  value determined in the presented work is thus in excellent agreement with the latter result and consistent within a  $1\sigma$  level with Campbell *et al.* [7].

In their work, Michel *et al.* [8] state that they have resolved the deviations from the Primakoff-Porter theory (predicting a  $Z^{-2}$  behavior of  $P_{KK}$ ), when comparing the result of Campbell *et al.* [7] with the later measurement of Hindi, White, and Kozub [31] for  $^{54}\text{Mn}$ . However, also Hindi, White, and Kozub [31] used the assumption of equal fluorescence yields for the hypersatellite, the satellite and the regular  $K$ -line photons. For  $Z = 24$ , we find  $\omega_{\text{H}} = 0.309$  [25],  $\omega_{\text{S}} = 0.289$  [26], and  $\omega_K = 0.258$  [11,32], and thus a corrected double vacancy production probability for  $^{54}\text{Mn}$  of  $P_{KK}(^{54}\text{Mn}) = (2.03_{-0.44}^{+0.71}) \times 10^{-4}$ . When extrapolated, this results in  $P_{KK}(^{55}\text{Fe}) = (1.87_{-0.41}^{+0.65}) \times 10^{-4}$ , which gives a ratio with the  $P_{KK}$  value obtained in the presented work of  $1.35_{-0.30}^{+0.47}$  with a systematic uncertainty of 0.04, which is almost consistent with 1 on a  $1\sigma$  confidence level. The discrepancy of the  $P_{KK}$  for  $^{65}\text{Zn}$  as measured by Nagy and Schupp [33] remains, if the  $Z^{-2}$  dependence of  $P_{KK}$  is assumed.

While the Primakoff-Porter theory predicts  $P_{KK}$  within a nonrelativistic hydrogenlike system, (semi)relativistic corrections of their theory showed large variations for different models. Table I in [7] gives an overview of calculated values for  $P_{KK}$ . In the present work we determined a value which

is not consistent with any of the theoretical predictions described therein. Our result is between the values obtained by the full many-body treatment based on a Dirac-Fock-Slater self-consistent field (SCF) potential ( $P_{KK} = 2.4 \times 10^{-4}$ ) [34] and the Coulomb propagator method ( $P_{KK} = 1.13 \times 10^{-4}$ ) [35], while favoring the latter model.

## V. CONCLUSION

The angular correlation function between the coincident hypersatellite-satellite emission after double  $K$ -shell ionization in electron capture of  $^{55}\text{Fe}$  was measured for the first time. From this the anisotropy parameter  $\beta_2^{\text{eff}}(\text{exp}) = 0.09656 \pm 0.05270$  was extracted, which is in very good agreement with the theoretical value of  $\beta_2^{\text{eff}}(\text{theor}) = 0.09735$ , obtained in electric dipole approximation by neglecting outer-shell electrons. The weight factors of involved fine-structure transitions were calculated following the multiconfiguration Dirac-Fock (MCDF) approach.

Moreover, by improving statistics and lowering systematic uncertainties, when compared to previous measurements, we

found  $P_{KK} = (1.388 \pm 0.037) \times 10^{-4}$  with a systematic error  $\Delta P_{KK, \text{sys}} = 0.042 \times 10^{-4}$ . The result is in agreement with earlier measurements. In particular, it confirms the result of our previous publication, where the discrepancies of measurements with  $^{54}\text{Mn}$ ,  $^{55}\text{Fe}$ , and  $^{65}\text{Zn}$  were partly resolved. None of the theoretical predictions including relativistic calculations were found to be consistent with the obtained  $P_{KK}$  value.

## ACKNOWLEDGMENTS

We thank the German metrology institute PTB for manufacturing and calibrating the radioactive source and the Medipix Collaboration for the development of the Timepix detector. This research project was supported by a Marie Curie Early Initial Training Network Fellowship of the European Community's Seventh Framework Programme under Grant Agreement PITN-GA-4 2011-289198-ARDENT. T.M. is grateful to the Deutsche Forschungsgemeinschaft (DFG) for funding the study on the use of pixel detectors for the coincident detection of x rays emerging from double electron captures.

- 
- [1] T. Schneider and J.-M. Rost, *Phys. Rev. A* **67**, 062704 (2003).
  - [2] J. P. Briand, P. Chevallier, M. Tavernier, and J. P. Rozet, *Phys. Rev. Lett.* **27**, 777 (1971).
  - [3] J. P. Briand, P. Chevalier, A. Johnson, J. P. Rozet, M. Tavernier, and A. Touati, *Phys. Lett. A* **49**, 51 (1974).
  - [4] G. Charpak, *Compt. Rend. Acad. Sci.* **237**, 243 (1953).
  - [5] M. M. Hindi and R. L. Kozub, *Phys. Rev. C* **45**, 1070 (1992).
  - [6] H. Primakoff and F. T. Porter, *Phys. Rev.* **89**, 930 (1953).
  - [7] J. L. Campbell, J. A. Maxwell, and W. J. Teesdale, *Phys. Rev. C* **43**, 1656 (1991).
  - [8] T. Michel, B. Bergmann, J. Durst, M. Filipenko, T. Gleixner, and K. Zuber, *Phys. Rev. C* **89**, 014609 (2014).
  - [9] S. Fritzsche, P. Indelicato, and T. Stöhlker, *J. Phys. B* **38**, S707 (2005).
  - [10] I. Žilimen, E. Browne, Y. Chan, M. T. F. da Cruz, A. García, R.-M. Larimer, K. T. Lesko, E. B. Norman, R. G. Stokstad, and F. E. Wietfeldt, *Phys. Rev. C* **46**, 1136 (1992).
  - [11] M. Be, V. Chiste, C. Dulieu, E. Browne, C. Baglin, V. Chechev, N. Kuzmenko, R. Helmer, F. Kondev, D. MacMahon, and K. Lee, *Table of Radionuclides*, Vol. 3, Monographie BIPM-5 (Bureau International des Poids et Mesures, Sèvres, 2006), pp. 5–28.
  - [12] E. L. Brady and M. Deutsch, *Phys. Rev.* **78**, 558 (1950).
  - [13] D. T. Stevenson and M. Deutsch, *Phys. Rev.* **83**, 1202 (1951).
  - [14] M. Campbell, *Nucl. Instrum. Methods Phys. Res., Sect. A* **633**, Suppl. 1, S1 (2011).
  - [15] V. Kraus, M. Holik, J. Jakubek, M. Kroupa, P. Soukup, and Z. Vykydal, *J. Instrum.* **6**, C01079 (2011).
  - [16] D. Turecek, T. Holy, J. Jakubek, S. Pospisil, and Z. Vykydal, *J. Instrum.* **6**, C01046 (2011).
  - [17] T. Holy, E. Heijne, J. Jakubek, S. Pospisil, J. Uher, and Z. Vykydal, *Nucl. Instrum. Methods Phys. Res., Sect. A* **591**, 287 (2008).
  - [18] J. Giersch, A. Weidemann, and G. Anton, *Nucl. Instrum. Methods Phys. Res., Sect. A* **509**, 151 (2003).
  - [19] U. Fano, *Phys. Rev.* **72**, 26 (1947).
  - [20] H. Spieler and E. Haller, *IEEE Trans. Nucl. Sci.* **32**, 419 (1985).
  - [21] S. Ramo, *Proc. IRE* **27**, 584 (1939).
  - [22] W. Shockley, *J. Appl. Phys.* **9**, 635 (1938).
  - [23] P. Sievers, T. Weber, T. Michel, J. Klammer, L. Büermann, and G. Anton, *J. Instrum.* **7**, P03003 (2012).
  - [24] J. G. Pengra and B. Crasemann, *Phys. Rev.* **131**, 2642 (1963).
  - [25] M. H. Chen, *Phys. Rev. A* **44**, 239 (1991).
  - [26] M. Kavcic, M. Budnar, and J. Campbell, *Nucl. Instrum. Methods Phys. Res., Sect. A* **196**, 16 (2002).
  - [27] M. H. Biavati, S. J. Nassiff, and C. S. Wu, *Phys. Rev.* **125**, 1364 (1962).
  - [28] M. C. Chon and J. Law, *Phys. Rev. A* **50**, 1372 (1994).
  - [29] A. Surzhykov, U. D. Jentschura, T. Stöhlker, and S. Fritzsche, *Phys. Rev. A* **73**, 032716 (2006).
  - [30] S. Fritzsche, *Comput. Phys. Commun.* **183**, 1525 (2012).
  - [31] M. M. Hindi, C. A. White, and R. L. Kozub, *Phys. Rev. C* **68**, 014306 (2003).
  - [32] M. Be, V. Chiste, C. Dulieu, E. Browne, C. Baglin, V. Chechev, N. Kuzmenko, R. Helmer, F. Kondev, D. MacMahon, and K. Lee, *Table of Radionuclides*, Vol. 1, Monographie BIPM-5 (Bureau International des Poids et Mesures, Sèvres, 2006), pp. 71–76.
  - [33] H. J. Nagy and G. Schupp, *Phys. Rev. C* **27**, 2887 (1983).
  - [34] A. Suzuki and J. Law, *Phys. Rev. C* **25**, 2722 (1982).
  - [35] R. L. Intemann, *Phys. Rev. C* **31**, 1961 (1985).